Instability wave-streak interactions in a hypersonic boundary layer at flight conditions

Pedro Paredes†, Meelan M. Choudhari, and Fei Li

Computational AeroSciences Branch, NASA Langley Research Center, Hampton, VA 23681, USA

The interaction of stationary streaks undergoing nonmodal growth with modally unstable instability waves in a hypersonic boundary-layer flow is studied using numerical computations. The geometry and flow conditions are selected to match a relevant trajectory location from the ascent phase of the HIFiRE-1 flight experiment; namely, a 7 degree half-angle, circular cone with 2.5 mm nose radius, freestream Mach number equal to 5.30, unit Reynolds number equal to 13.42 m^{-1}, and wall-to-adiabatic temperature ratio of approximately 0.35 over most of the vehicle. This paper investigates the nonlinear evolution of initially linear optimal disturbances that evolve into finite-amplitude streaks, followed by an analysis of the modal instability characteristics of the perturbed, streaky boundary-layer flow. The investigation is performed with stationary direct numerical simulations (DNS) and plane-marching parabolized stability equations (PSE), in conjunction with partial-differential-equation-based planar eigenvalue analysis. The overall effect of streaks is to reduce the peak amplification factors of instability waves, indicating a possible downstream shift in the onset of laminar-turbulent transition. The present study confirms previous findings that the mean flow distorsion of the nonlinear streak perturbation reduces the amplification rates of the Mack-mode instability. More importantly, however, the present results demonstrate that the spanwise varying component of the streak can produce a larger effect on the Mack-mode amplification. The study with selected azimuthal wavenumbers for the stationary streaks reveals that a wavenumber of approximately 1.4 times larger than the optimal wavenumber is more effective in stabilizing the planar Mack-mode instabilities. In the absence of unstable first-mode waves for the present cold-wall condition, transition onset is expected to be delayed until the peak streak amplitude increases to nearly 35 percent of the freestream velocity, when intrinsic instabilities of the boundary-layer streaks begin to dominate the transition process. For streak amplitudes below that limit a significant net stabilization is achieved, yielding a potential transition delay that can exceed 100 percent of the length of the laminar region in the uncontrolled case.

1. Introduction

Laminar-turbulent transition of boundary-layer flows can have a strong impact on the performance of hypersonic vehicles because of its influence on the surface skin friction and aerodynamic heating. Therefore, the prediction and control of transition onset and the associated variation in aerothermodynamic parameters in high-speed flows is a key issue for optimizing the performance of the next-generation aerospace vehicles.

Under low levels of background disturbances, transition is initiated by the exponential

† Email address for correspondence: pedro.paredes@nasa.gov

amplification of linearly unstable eigenmodes, i.e., modal instabilities of the laminar boundary layer. In two-dimensional boundary layers, different instability mechanisms dominate the exponential growth phase depending on the flight speed. Planar, i.e., two-dimensional, Tollmien-Schlichting (TS) waves are the most unstable in the incompressible regime, whereas oblique first-mode instabilities correspond to the most amplified disturbances in supersonic boundary layers. The hypersonic regime is again dominated by the growth of planar acoustic waves of the second mode, i.e., Mack-mode type (Mack 1984). In the presence of sufficiently strong external disturbances in the form of either freestream turbulence (FST) or three-dimensional wall roughness, streamwise streaks involving alternately low and high streamwise velocity have been observed to appear in incompressible boundary layers (Klebanoff 1971; Vermeersch & Arnal 2010). Further research in the incompressible regime has shown that high amplitude streaks can become unstable to shear layer instabilities that lead to a form of "bypass transition" (Andersson *et al.* 2001). When the streak amplitudes are low enough to avoid these instabilities, i.e., when the background disturbance level is moderate, the streaks can actually reduce the growth of the TS waves as documented in both theoretical and experimental studies (Boiko *et al.* 1994; Cossu & Brandt 2002; Bagheri & Hanifi 2007). The stabilizing effect of stationary streaks in low-speed boundary layers have been used in passive flow control strategies to demonstrate delayed onset of transition by using micro vortex generators (MVGs) along the body surface (Fransson *et al.* 2006; Shahinfar *et al.* 2012).

Despite the numerous research efforts focused on tripping hypersonic boundary-layer flows by using roughness elements, there have been a few experimental and numerical studies reporting a delay in transition under certain circumstances. Most of these studies used two-dimensional roughness elements. James (1959) used fin-stabilized hollow tube models in free flight with a screw-thread type of distributed two-dimensional roughness. He found that for a given freestream Mach number between the range of 2.8 to 7, there exists an optimum roughness height for transition delay. Fujii (2006) studied the effects of two-dimensional roughness by using a 5° half-angle sharp cone at a freestream Mach number of 7.1. He also observed transition delay for certain conditions when the wavelength of the wavy wall roughness was comparable to that of the Mack-mode instabilities. More recently, Fong *et al.* (2014, 2015) performed numerical and experimental studies, respectively, that were focused on the effect of two-dimensional surface roughness on the stability of a hypersonic boundary layer at a freestream Mach number of 6. The experiments (Fong *et al.* 2015) used a flared cone with strips of roughness in the Boeing/AFOSR Mach 6 Quiet Tunnel and supported the numerical predictions indicating a stabilizing influence on the amplification of Mack-mode disturbances (Fong *et al.* 2014). In particular, these studies showed that the most dominant Mack-mode instability could be suppressed via judicious placement of the roughness elements along the surface of the cone. Among the limited experimental evidence of delayed transition in a hypersonic boundary layer and in the presence of three-dimensional roughness elements is the study by Holloway & Sterrett (1964), who used a single row of spherical roughness elements partially recessed within a flat plate model in the NASA Langley 20-inch Mach 6 tunnel. Data for multiple boundary-layer-edge Mach numbers were obtained by varying the plate mounting angle. They found that, for cases with the smallest roughness diameters, transition was delayed for edge Mach numbers larger than 3.7, which approximately corresponds to the lower bound for second-mode dominance over first-mode instabilities in a flat plate boundary layer at typical wind tunnel conditions. Therefore, their results are suggestive of a stabilizing influence of roughness-induced streaks on Mack-mode waves. When the roughness height becomes sufficiently large, the streaks can develop

high-frequency instabilities that can lead to earlier transition (Choudhari *et al.* 2009; Paredes *et al.* 2015*a*) as found by Holloway & Sterrett (1964).

Theoretical studies of the interaction between stationary disturbances and Mack-mode instabilities in hypersonic boundary layers have been recently initiated. Li *et al.* (2010) studied the interaction of Goertler vortices with Mack-mode instabilities on a flared cone, demonstrating a possible route to transition via this interaction. Li *et al.* (2015*b*) studied the secondary instability of crossflow vortices in a hypersonic cone at angle of attack and found that nonlinearly saturated crossflow vortices destabilize the Mack modes, which dominate the transition onset over the intrinsic secondary instabilities of the crossflow vortices (Choudhari *et al.* 2017, 2018). Ren *et al.* (2016) studied the stabilizing effect of weakly nonlinear suboptimal streaks and Goertler vortices on the planar first-mode and Mack-mode instabilities. They documented a slight reduction in the logarithmic amplification factor of approximately $\Delta N = 0.2$ relative to the baseline, zero-streaks flat plate boundary layer. Furthermore, Paredes *et al.* (2016*b*, 2017*b*) have demonstrated that finite-amplitude optimal streaks can substantially damp planar Mack-mode instabilities in the hypersonic flow over a circular cone at zero angle of attack and ground test conditions, although oblique first-mode instabilities are destabilized.

The development of roughness-induced streaks is strongly dependent on the details of roughness element shape, height, and spanwise or azimuthal spacing. A conceptually simple model that can characterize as well as provide an upper bound on the transient algebraic growth and subsequent slow decay of boundary-layer streaks due to arbitrary initial disturbances is the optimal growth theory; see Schmid (2007) for a review. The transient growth arises as a result of the non-normality of disturbance equations, and the optimal growth theory seeks to maximize the disturbance growth between a selected pair of streamwise locations. Regardless of the flow Mach number, the disturbances experiencing the highest magnitude of transient growth have been found to be stationary streaks that arise from initial perturbations that correspond to streamwise vortices. The instabilities of optimal streaks with finite initial amplitudes in supersonic and hypersonic boundary layers has been recently addressed by Paredes *et al.* (2016*a*,*c*, 2017*c*). Furthermore, Paredes *et al.* (2017*a*) investigated the interaction of nonlinear stationary optimal growth perturbations with modally unstable instability waves in a Mach 3 adiabatic flat-plate boundary-layer flow. At the selected conditions, the most-amplified linear waves correspond to the oblique, first-mode waves. The analysis showed that optimally growing stationary streaks can destabilize the first-mode waves, but only when the spanwise wavelength of the instability waves is equal to or smaller than twice the streak spacing. Thus, as long as the amplification factors for the destabilized, short wavelength instability waves remain below the threshold level for transition, a significant net stabilization is achieved. On the other hand, the effect of nonlinear stationary streaks on the growth of Mack-mode instabilities has not been studied as yet. The present work seeks to bridge this gap with the goal of developing a more thorough knowledge base for transition prediction in the presence of stationary streaks and potentially expand the range of available techniques for transition control at hypersonic flight Mach number conditions.

To that end, we study the effect of a periodic array of finite-amplitude streaks on the dominant instability waves in axisymmetric or two-dimensional boundary layers at hypersonic Mach numbers, i.e., the Mack-mode instabilities. Figure 1 shows a schematic of the flow configuration considered in this work. The geometry is a 7° half-angle circular cone with $r_n = 2.5$ mm nose radius and $L_c = 2.0$ m length. The freestream parameters ($M = 5.3$, $Re' = 13.42 \times 10^6$ m^{-1}, $T^*_\infty = 201.4$ K) are selected to match the flow conditions of the HIFiRE-1 flight experiment during the ascent phase at time

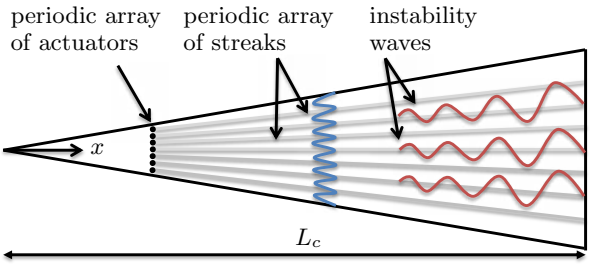

FIGURE 1. Sketch (side view) of the cone illustrating the present conceptual configuration. The wake of the periodic array of actuators generate the periodic array of streaks that modulate the instability waves.

equal to 21.5 s (Kimmel *et al.* 2015). The laminar boundary layer flow is computed by solving the full Navier-Stokes equations. The good correlation between experimental measurements and theoretical predictions based on the parabolized stability equations (PSE) has confirmed that laminar-turbulent transition in this flow is driven by the modal growth of planar Mack-mode instabilities (Li *et al.* 2015*a*). The analysis presented herein is based on boundary-layer streaks resulting from the transient growth of an optimal initial perturbation. The perturbed three-dimensional boundary layer is used as a basic state for the subsequent modal instability analysis by means of the plane-marching PSE.

The paper is organized as follows. Section 2 provides a summary of the transient growth framework and the plane-marching PSE. The results are presented in §3. First, the perturbed three-dimensional boundary layer composed of the two-dimensional boundary layer plus a finite-amplitude optimal growth perturbation is analyzed by using the stationary from of the plane-marching PSE. Subsequently, the plane marching PSE are used to examine the instability characteristics of the Mack-mode waves as well as the streak instabilities of the modified basic states. The effect of the streak azimuthal wavelength on the net stabilization of the Mack-mode waves is also studied in §3. Finally, summary and concluding remarks are presented in §4.

2. Theory

This section introduces the methodologies used in this paper. The procedure closely follows the study of Paredes *et al.* (2017*a*) that analyzed the interactions of the oblique first-mode waves and finite-amplitude optimal streaks in a supersonic boundary layer. In brief, the analysis begins with the identification of the linearly optimal perturbation that results in maximum energy gain. The latter is then used as inflow disturbance for the parabolic integration of the stationary, nonlinear, plane-marching PSE to obtain a three-dimensional, azimuthally-periodic, perturbed boundary-layer flow. Subsequently, the modal instability characteristics of this perturbed three-dimensional boundary-layer flow are studied by using the linear form of time harmonic, plane-marching PSE.

2.1. *Linear optimal growth*

Linear transient growth analysis is performed using the linear PSE as explained by Pralits *et al.* (2000) and Paredes *et al.* (2016*d*). In the PSE context, the perturbations have the form

$$\tilde{\mathbf{q}}(\xi,\eta,\zeta,t) = \hat{\mathbf{q}}(\xi,\eta)\exp\left[\mathrm{i}\left(\int_{\xi_0}^{\xi}\alpha(\xi')\,\mathrm{d}\xi' + m\zeta - \omega t\right)\right]. \tag{2.1}$$

The suitably nondimensionalized, orthogonal, curvilinear coordinate system (ξ, η, ζ) denotes streamwise, wall-normal, and azimuthal coordinates and (u, v, w) represent the corresponding velocity components. Density and temperature are denoted by ρ and T. The Cartesian coordinates are represented by (x, y, z). The vector of perturbation fluid variables is $\tilde{\mathbf{q}}(\xi, \eta, \zeta, t) = (\tilde{\rho}, \tilde{u}, \tilde{v}, \tilde{w}, \tilde{T})^T$, the vector of amplitude functions is $\hat{\mathbf{q}}(\xi, \eta) = (\hat{\rho}, \hat{u}, \hat{v}, \hat{w}, \hat{T})^T$, and the vector of basic state fluid variables is $\bar{\mathbf{q}}(\xi, \eta) = (\bar{\rho}, \bar{u}, \bar{v}, \bar{w}, \bar{T})^T$. The streamwise and azimuthal wavenumbers are α and m, respectively; and ω is the angular frequency of the perturbation. The azimuthal wavelength is defined as $\lambda = 2\pi/m$.

The optimal initial disturbance, $\tilde{\mathbf{q}}_0$, is defined as the initial (i.e., inflow) condition at ξ_0 that yields a maximum objective function, $J(\tilde{\mathbf{q}})$. The objective function is defined as the energy gain of the perturbation up to a specified position, ξ_1. Herein, we use the mean energy gain,

$$G = \frac{1}{\xi_1 - \xi_0} \frac{\int_{\xi_0}^{\xi_1} E(\xi') \mathrm{d}\xi'}{E(\xi_0)}, \tag{2.2}$$

where E denotes the energy norm of $\tilde{\mathbf{q}}$. The energy norm is defined as

$$E(\xi) = \frac{1}{\lambda} \int_{\zeta} \int_{\eta} \tilde{\mathbf{q}}(\xi, \eta, \zeta)^H \mathbf{M} \tilde{\mathbf{q}}(\xi, \eta, \zeta)\, h_\xi\, h_\zeta \,\mathrm{d}\eta \,\mathrm{d}\zeta, \tag{2.3}$$

where h_ξ and h_ζ are the metric factors associated with the streamwise and azimuthal curvatures, respectively, $\mathbf{M}$ is the energy weight matrix and the superscript H denotes conjugate transpose. The positive-definite energy norm used here was derived by Mack (1969) and Hanifi *et al.* (1996) and is defined as

$$\mathbf{M} = \mathrm{diag}\left[\frac{\bar{T}(\xi, \eta)}{\gamma \bar{\rho}(\xi, \eta) M^2}, \bar{\rho}(\xi, \eta), \bar{\rho}(\xi, \eta), \bar{\rho}(\xi, \eta), \frac{\bar{\rho}(\xi, \eta)}{\gamma(\gamma - 1)\bar{T}(\xi, \eta) M^2}\right]. \tag{2.4}$$

The variational formulation of the problem to determine the maximum of the objective functional $J = G$ leads to an optimality system (Pralits *et al.* 2000; Tumin & Reshotko 2003; Zuccher *et al.* 2006), which is solved in an iterative manner starting from a random solution at ξ_0 that must satisfy the boundary conditions. Summarizing, the linear PSE, $\mathbf{L}\tilde{\mathbf{q}} = 0$, are used to integrate $\tilde{\mathbf{q}}$ up to ξ_1, where the final optimality condition is used to obtain the initial condition for the backward adjoint PSE integration. At ξ_0, the adjoint solution is used to calculate the new initial condition for the forward PSE integration with the initial optimality condition. The iterative procedure finishes when the value of J has converged up to a certain tolerance, which was set to a relative error of 10^{-6} in the present computations.

2.2. *Plane-marching PSE*

The nonlinear evolution of the stationary, finite-amplitude streaks is solved using an implicit formulation of the nonlinear plane-marching PSE (Paredes *et al.* 2015*b*, 2016*c*, 2017*a*). Subsequently, the linear form of the plane-marching PSE is used to study the linear, nonparallel stability characteristics of the modified basic state corresponding to the sum of the circular cone boundary layer and the finite-amplitude optimal disturbance. The initial disturbance profiles for the plane-marching PSE are obtained using a partial-differential-equation (PDE) based two-dimensional eigenvalue problem (EVP). In the plane-marching PSE context, the perturbations to the streak have the form

$$\tilde{\mathbf{q}}(\xi, \eta, \zeta, t) = \hat{\mathbf{q}}(\xi, \eta, \zeta) \exp\left[\mathrm{i}\left(\int_{\xi_0}^{\xi} \alpha(\xi')\,\mathrm{d}\xi' - \omega t\right)\right]. \tag{2.5}$$

A more detailed description of the plane-marching PSE methodology is given by Paredes (2014), Paredes *et al.* (2015*b*) and Paredes *et al.* (2017*a*).

The onset of laminar-turbulent transition is estimated using the logarithmic amplification ratio, the so-called N-factor, based on the Mack's energy norm E defined in Eq. (2.3) and relative to the lower bound location ξ_{lb} where the disturbance first becomes unstable,

$$N = -\int_{\xi_{lb}}^{\xi} \alpha_i(\xi')\,\mathrm{d}\xi' + 1/2 \ln\left[\hat{E}(\xi)/\hat{E}(\xi_{lb})\right]. \tag{2.6}$$

Accordingly, we assume that transition onset is likely to occur when the peak N-factor reaches a specified value. Similarly, the nonparallel growth rate based on the Mack's energy norm E is defined as

$$\sigma = \frac{\mathrm{d}N}{\mathrm{d}\xi}. \tag{2.7}$$

2.3. *Spatial discretization and boundary conditions*

The PSE are integrated along the streamwise coordinate by using second-order backward differentiation. A constant step of $\Delta R = 2.5$, where $R = \sqrt{Re_x}$, along the streamwise direction is used. Finite differences (Hermanns & Hernández 2008; Paredes *et al.* 2013) (FD-q) of sixth-order are used for discretization of the wall-normal coordinate. In the transient growth computations with PSE, the wall-normal direction is discretized using $N_\eta = 201$. The nodes are clustered towards the wall (Paredes *et al.* 2013). The clustering of points is dependent on the boundary layer thickness, with half of the grid points located below $10 \times \delta$, where δ is the similarity scale. No-slip, isothermal boundary conditions are used at the wall, i.e., $\hat{u} = \hat{v} = \hat{w} = \hat{T} = 0$. The amplitude functions are forced to decay at the farfield boundary by imposing the Dirichlet conditions $\hat{\rho} = \hat{u} = \hat{w} = \hat{T} = 0$. The farfield boundary coordinate is set just below the shock layer.

The plane-marching PSE are used to predict the nonlinear evolution of finite-amplitude transient growth disturbances as well as the linear amplification characteristics of modulated Mack-mode waves and streak instability waves sustained by the nonlinear streak disturbances. The plane-marching PSE are integrated using the same streamwise and wall-normal discretizations as that of the linear optimal growth analysis by using classic PSE, although depending on the initial amplitude, the number of wall-normal nodes is increased up to $N_\eta = 241$. In addition to the streamwise and wall-normal directions, the azimuthal direction is discretized with Fourier collocation points. Note that the PSE amplitude function of Eq. (2.1), $\hat{\mathbf{q}}(\xi, \eta)$, depends only on the streamwise and wall-normal coordinates, while that corresponding to plane-marching of Eq. (2.5), $\hat{\mathbf{q}}(\xi, \eta, \zeta)$ depends on all three spatial directions. Depending on the amplitude of the optimal growth perturbation, the number of azimuthal points is varied from $N_\zeta = 16$ to $N_\zeta = 64$. Similar to the streamwise and wall-normal grids, the same azimuthal grids are used to compute the evolution of both finite-amplitude streaks and their modal instabilities. However, a nonperiodic finite-difference discretization (FD-q) of sixth-order is also used in the azimuthal direction during a subset of the calculations for improved computational efficiency. With the nonperiodic scheme, only one half of the streak azimuthal wavelength, $\lambda_{ST} = 2\pi/m_{ST}$, where m_{ST} denotes the streak wavenumber, needs to be discretized and the boundary conditions in $\zeta = 0$ and $\zeta = \lambda_{ST}/2$ determine the instability mode to be studied, i.e., sinuous (S) or varicose (V) mode types with a fundamental ($m = m_{ST}$), subharmonic ($m = 1/2\, m_{ST}$), and $m = 3/2\, m_{ST}$ wavenumbers. Table 1 shows the boundary conditions used in each case.

The number of discretization points in all three directions and the wall-normal domain

wavenumber ($\times m_{ST}$)	mode type	$\zeta = 0$	$\zeta = \lambda_{ST}/2$
1	S	$(\hat{\rho}\ ,\hat{u}\ ,\hat{v}\ ,\hat{w}_\zeta,\hat{T}\ )^T = \mathbf{0}$	$(\hat{\rho}\ ,\hat{u}\ ,\hat{v}\ ,\hat{w}_\zeta,\hat{T}\ )^T = \mathbf{0}$
1	V	$(\hat{\rho}_\zeta,\hat{u}_\zeta,\hat{v}_\zeta,\hat{w}\ ,\hat{T}_\zeta)^T = \mathbf{0}$	$(\hat{\rho}_\zeta,\hat{u}_\zeta,\hat{v}_\zeta,\hat{w}\ ,\hat{T}_\zeta)^T = \mathbf{0}$
1/2, 3/2	S	$(\hat{\rho}_\zeta,\hat{u}_\zeta,\hat{v}_\zeta,\hat{w}\ ,\hat{T}_\zeta)^T = \mathbf{0}$	$(\hat{\rho}\ ,\hat{u}\ ,\hat{v}\ ,\hat{w}_\zeta,\hat{T}\ )^T = \mathbf{0}$
1/2, 3/2	V	$(\hat{\rho}\ ,\hat{u}\ ,\hat{v}\ ,\hat{w}_\zeta,\hat{T}\ )^T = \mathbf{0}$	$(\hat{\rho}_\zeta,\hat{u}_\zeta,\hat{v}_\zeta,\hat{w}\ ,\hat{T}_\zeta)^T = \mathbf{0}$

TABLE 1. Azimuthal boundary conditions used in the plane-marching PSE analysis. The mode types S and V refer to sinuous and varicose mode shapes, respectively, with respect to the half symmetry plane of the streak, $\zeta = \lambda_{ST}/2$. Also, note that $q_\zeta \equiv \partial q/\partial\zeta$.

size were varied to ensure that the relevant flow quantities were insensitive to further improvement in grid resolution and enlargement of the domain size. Verification of the present linear optimal growth module against available transient growth results from the literature is shown in Paredes *et al.* (2016*d*). Verification of the present plane-marching PSE module against line-marching PSE and DNS results is shown in De Tullio *et al.* (2013) and Paredes *et al.* (2015*b*).

3. Results

Next, we study the axisymmetric boundary layer over a nearly sharp, 7° half-angle circular cone at zero angle of attack in a hypersonic freestream flow. The details of the basic state and its modal instability characteristics are introduced first. Then, the linear transient growth analysis and the evolution of finite-amplitude optimal perturbations are presented. Finally, the instability characteristics of the perturbed boundary-layer flows and the overall effects of the streaks on the estimated transition onset location are analyzed.

3.1. *Basic state solution*

The present analysis is performed for a 7° half-angle circular cone at zero angle of attack in a hypersonic freestream flow. The length of the nearly sharp cone is $L_c^* = 2.0$ m, and the nose radius is $r_n^* = 2.5$ mm so that the front half of the cone matches the HIFiRE-1 geometry. The extended cone length is used in the present investigation to assess the extent of potential delay in laminar-turbulent transition due to the streaks. The basic state, laminar boundary-layer flow over the cone surface is computed by using a second-order accurate algorithm as implemented in the finite-volume compressible Navier-Stokes flow solver VULCAN-CFD† (Litton *et al.* 2003). The VULCAN-CFD solution is based on the full Navier-Stokes equations and uses the solver's built-in capability to iteratively adapt the computational grid to the shock. Sutherland's law is assumed for bulk viscosity.

The freestream conditions are selected to replicate those of the HIFiRE-1 flight experiment at time equal to 21.5 s during the ascent phase (Kimmel *et al.* 2015), i.e., Mach 5.30 flow with a unit Reynolds number of 13.42×10^6 m^{-1}, freestream temperature of $T_\infty^* = 201.4$ K and a prescribed surface temperature distribution that corresponds to a wall-to-adiabatic temperature ratio of approximately 0.35 over most of the vehicle (Li *et al.* 2015*a*). Figure 2(a) shows the prescribed wall temperature along the surface of the cone. As explained by Li *et al.* (2015*a*), the surface temperature distribution was obtained by combining the results of thermal analysis based on axisymmetric, finite-

† visit `http://vulcan-cfd.larc.nasa.gov` for further information about the VULCAN-CFD solver

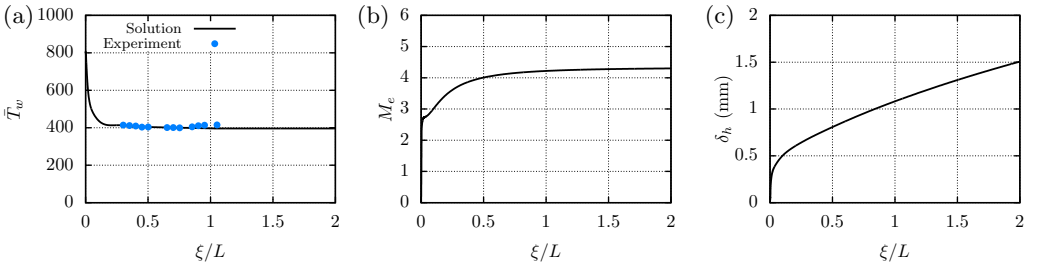

FIGURE 2. Streamwise evolution of (a) wall temperature, (b) edge Mach number, and (c) boundary layer thickness. The wall temperature values measured in the flight experiments are included.

element calculations using the U.S. Air Force Research Laboratory (AFRL) TOPAZ code (Kimmel *et al.* 2007) and the experimental data based on thermocouple measurements (Kimmel *et al.* 2015). The edge Mach number M_e and boundary layer thickness δ_h, which is defined as the wall-normal position where $h_t/h_{t,\infty} = 0.995$, where h_t is the total enthalpy, are plotted in figures 2(b) and 2(c), respectively.

The computational grid has 865 points in the streamwise direction and 513 points in the wall normal direction. A minimum of 120 points is clustered next to the cone surface to resolve the thickness of the boundary layer. This grid resolution is based on the work of Li *et al.* (2015*a*), who computed the laminar flow over the HIFiRE-1 geometry at selected flight experiment conditions with the VULCAN-CFD solver and performed a grid-convergence test by doubling the number of points in each directions and a verification of the results by comparing the solution with that computed with a different Navier-Stokes solver, i.e., the CFL3D code (Rumsey *et al.* 1997).

In what follows, freestream values are used as reference values for nondimensionalization. The reference length scale is defined as $\delta = \sqrt{L\nu/u_\infty}$, where $L^* = 1.0$ m. For this problem, the computational coordinates, (ξ, η, ζ), are defined as an orthogonal body-fitted coordinate system. The metric factors are defined as

$$h_\xi = 1 + \kappa\eta, \tag{3.1}$$

$$h_\zeta = r_b + \eta\cos(\theta), \tag{3.2}$$

where κ denotes the streamwise curvature, r_b is the local radius, and θ is the local half-angle along the axisymmetric surface, i.e., $\sin(\theta) = \mathrm{d}r_b/\mathrm{d}\xi$. For the present straight circular cone (with exception of the nose region that is not included in this analysis), $\kappa \equiv 0$ and θ is the cone half-angle equal to 7°.

3.2. *Modal instability characteristics of the unperturbed flow*

Experimental measurements and theoretical predictions based on PSE have confirmed that laminar-turbulent transition in this flow is driven by the modal growth of planar Mack-mode instabilities (Li *et al.* 2015*a*). The instability of the unperturbed flow was examined by PSE to establish the transition behavior in the absence of stationary streak perturbations. The onset of laminar-turbulent transition in the unperturbed boundary-layer flow is estimated using N-factor evolution of the planar Mack modes computed with the PSE. For the conditions of the experiment (Kimmel *et al.* 2015), transition onset in the unperturbed cone boundary layer was measured to occur near $\xi_{tr}/L = 0.85$ m. Figure 3(a) shows that the peak N-factor at the measured transition location corresponds to $N_{tr} = 14.7$, which is reached by a planar Mack-mode disturbance with frequency $\omega = 0.603$. Figure 3(b) shows the growth-rate isolines of planar Mack-mode instabilities.

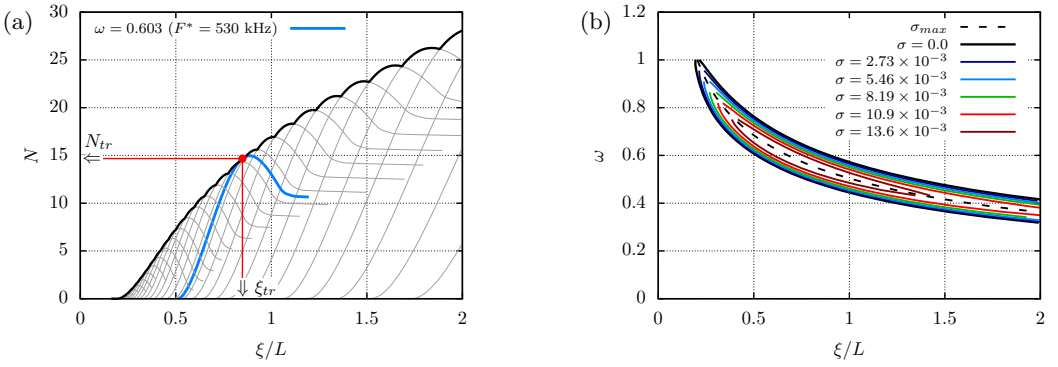

FIGURE 3. (a) N-factors and (b) growth-rate isolines of planar Mack-mode disturbances in the unperturbed boundary layer. The thick blue line in (a) denotes the mode that reaches largest N-factor value (N_{tr}) at the experimentally measured transition location (x_{tr}) and corresponds to a disturbance frequency of $\omega = 0.603$.

The neutral stability curve corresponds to the black line with $\sigma = 0.0$. Neither planar nor oblique first-mode instabilities were found in the present boundary-layer flow because of the low surface temperature relative to the adiabatic temperature.

3.3. *Stationary transient growth and streak development*

Herein, transient growth calculations are performed with the initial and final disturbance locations set to $\xi_0/L = 0.5$ and $\xi_1/L = 1.1$, respectively. The initial location ξ_0 has been selected near the first neutral branch of the planar Mack mode that first reaches N_{tr} (see figure 3(a)). The range $[\xi_0, \xi_1]$ has been chosen to obtain appreciable streak amplitudes over a majority of the cone length, as will be shown in what follows.

Linear transient growth predictions are presented first. Figure 4(a) shows the mean energy gain as a function of the azimuthal wavenumber. The optimal azimuthal wavenumber corresponding to maximum energy gain is found to be equal to $m_{op} = 180$. The components of the initial optimal perturbation with azimuthal wavenumbers of $m = 90$, 180, and 360 are plotted in figures 4(b), 4(c), and 4(d), respectively. Larger azimuthal wavenumbers lead to optimum initial profiles with a slightly shorter wall-normal extension than the initial profiles for lower wavenumbers. Furthermore, the peaks of the initial profiles with larger azimuthal wavenumbers are located slightly closer to the wall.

The nonlinear form of the plane-marching PSE is used to monitor the nonlinear development of optimal initial disturbances with specified amplitudes. These disturbances evolve into streamwise elongated streaks; and Figure 5(a) shows the evolution of the streak amplitude based on $\tilde{u}$,

$$As_u(\xi) = \frac{1}{2}[\max_{\eta,\zeta}(\tilde{u}(\xi,\eta,\zeta)) - \min_{\eta,\zeta}(\tilde{u}(\xi,\eta,\zeta))], \tag{3.3}$$

for selected initial amplitudes of the $m = 180$ disturbance from figure 4(c). Unlike the energy norm in Eq. (2.3), the velocity amplitude As_u is expected to be more closely related to the growth of streak instabilities. The streak amplitude parameter A corresponds to the maximum streak amplitude As_u achieved by a linear perturbation with the same initial amplitude, which is given by

$$A_0 = A \times \sqrt{E_{lin,A=1}}. \tag{3.4}$$

As indicated by Eq. (3.4), the amplitude parameter A provides a convenient measure of the initial disturbance amplitude. As seen in figure 5(a), nonlinear effects reduce the

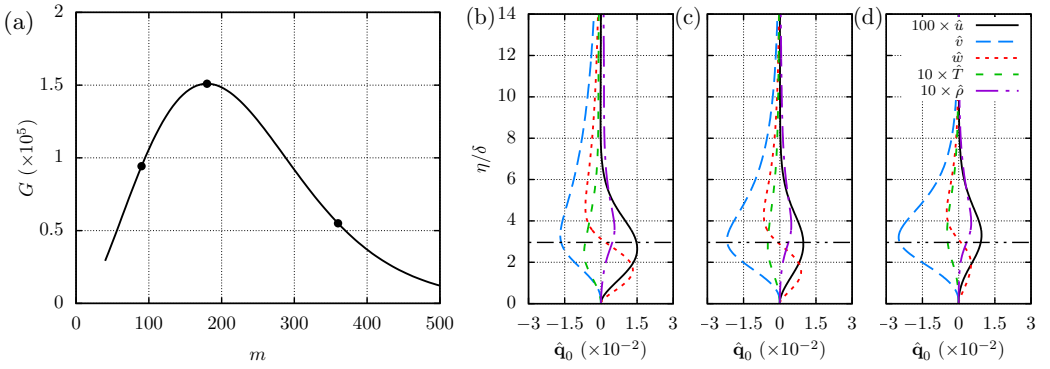

FIGURE 4. (a) Linear optimal mean energy gain, G, for initial and final disturbance locations at $\xi_0/L = 0.5$ and $\xi_1/L = 1.1$, respectively. Also, initial optimal amplitude vectors for (b) $m = 90$, (c) $m = 180$, and (d) $m = 360$. The horizontal, dash-double dot line in parts (b) through (d) indicates the edge of the boundary layer based on total enthalpy ($h_t/h_{t,\infty} = 0.995$).

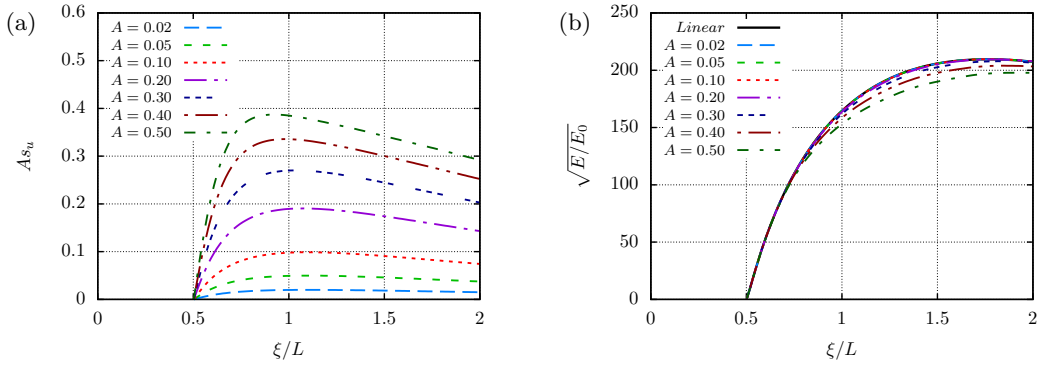

FIGURE 5. (a) Evolution of streak amplitudes based on u, As_u, and (b) evolution of disturbance amplitude, $\sqrt{E/E_0}$, of finite-amplitude, linear optimal perturbations initialized at $\xi_0/L = 0.5$ with $\xi_1/L = 1.1$ and $m = 180$.

streak amplitude relative to the linear prediction; hence, for any given case, $\max(As_u) < A$. The streamwise location of this maximum moves progressively upstream as the amplitude parameter A is increased. Figure 5(b), shows the evolution of the disturbance amplitude defined as the square root of the energy norm defined in Eq. (2.3) normalized by the initial energy. The deviation from the linear trend starts to become noticeable for $A \geqslant 0.20$.

Figures 6(a-d), 6(e-h), and 6(i-l) show the isocontours of the total streamwise velocity component in the cross-planes at selected streamwise locations for $A = 0.10$, $A = 0.20$, and $A = 0.40$, respectively. At the symmetry plane, $\zeta = \lambda_{ST}/2$, the near-wall, low-momentum fluid is lifted upward by the counter-rotating vortices, resulting in a localized region of increased boundary-layer thickness and lower wall shear. At the lateral symmetry plane, $\zeta = 0$ (or equivalently, $\zeta = \lambda_{ST}$), the effect of the initial streamwise vortices is exactly the opposite, yielding a localized region of reduced boundary-layer thickness and increased wall shear. As the streak amplitude becomes larger, the associated azimuthal gradients in the form of a detached three-dimensional shear-layer can support the growth of streak instabilities, as studied by Paredes *et al.* (2016*a*,*c*, 2017*c*), in the context of bypass transition in supersonic and hypersonic boundary layers.

Finally, the effect of streaks on the skin friction coefficient is studied in figure 7.

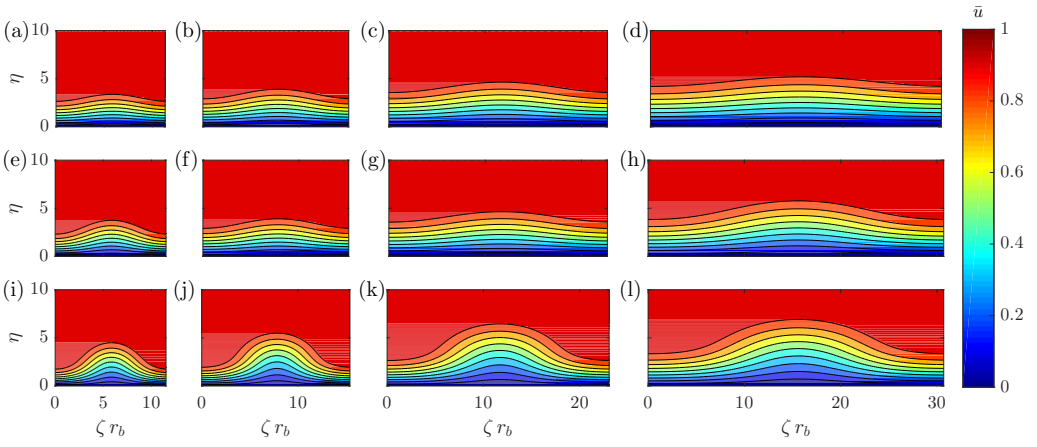

FIGURE 6. Isocontours of streamwise velocity with isolines at $\bar{u} = 0 : 0.1 : 0.9$ for streak amplitude parameters equal to (a,b,c,d) $A = 0.10$, (e,f,g,h) $A = 0.20$, and (i,j,k,l) $A = 0.40$, and streamwise locations equal to (a,e,i) $\xi/L = 0.75$, (b,f,j) $\xi/L = 1.00$, (c,g,k) $\xi/L = 1.50$, and (d,h,l) $\xi/L = 2.00$.

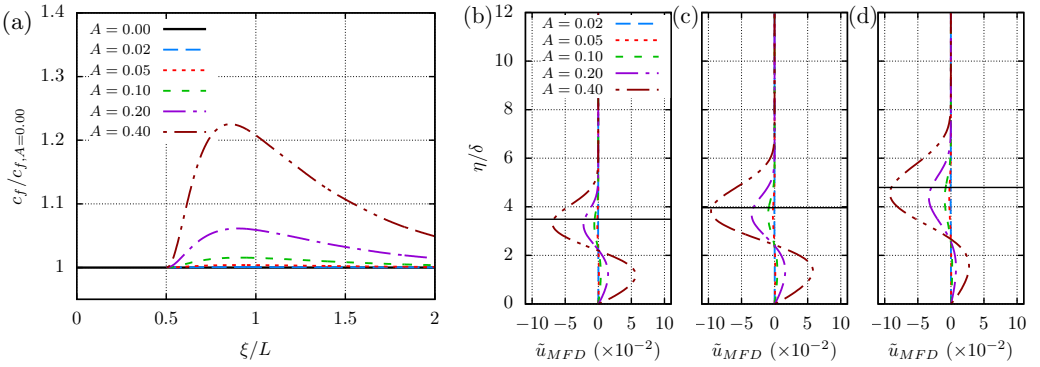

FIGURE 7. (a) Evolution of spanwise-averaged local skin friction coefficient ratio between those corresponding to perturbed flows and unperturbed flow, $c_f/c_{f,A=0.00}$. Also, mean-flow-distortion streamwise velocity profiles ($\tilde{u}_{MFD}$) at streamwise positions (b) $\xi/L = 0.75$, (c) 1.0, and (d) 1.5. The horizontal, solid black line in parts (b) through (d) indicates the edge of the unperturbed boundary layer based on total enthalpy ($h_t/h_{t,\infty} = 0.995$).

Figure 7(a) shows the ratio of the spanwise-averaged local skin friction coefficient with respect to that in the unperturbed case ($A = 0.00$). A peak skin friction increment of 6.1% is observed for the $A = 0.20$ case and of 22.5% for the $A = 0.40$ case. The skin friction coefficient is calculated with the wall normal gradient of the mean flow distortion (MFD) of the streamwise velocity perturbation, $\tilde{u}_{MFD}$, which is defined as

$$\tilde{u}_{MFD}(\xi,\eta) = \frac{1}{\lambda_{ST}} \int_0^{\lambda_{ST}} \tilde{u}(\xi,\eta,\zeta)\, \mathrm{d}\zeta. \tag{3.5}$$

Figures 7(b), 7(c), and 7(d) show the MFD streamwise velocity perturbation profiles at streamwise locations $\xi/L = 0.75$, 1.0, and 1.5, respectively. The profiles exhibit a positive peak close to the wall and a negative peak in the vicinity of the boundary-layer edge. The negative peak grows from $\xi/L = 0.75$ to $\xi/L = 2.0$, although the positive peak of $\tilde{u}_{MFD}$ decreases as the skin friction coefficient decreases from $\xi/L \approx 0.85$.

3.4. *Modal instability characteristics of the perturbed flow with optimal disturbances*

The instability characteristics of the modified, streaky boundary-layer flow are examined next. First, the streaks plotted in figure 5 corresponding to finite-amplitude linearly optimal disturbances initiated at $\xi_0/L = 0.5$ with $\xi_1/L = 1.1$ and $m_{ST} = 180$ are studied. After that, the effect of the streak azimuthal wavenumber m_{ST} on the net stabilization of Mack-mode waves is analyzed.

3.4.1. *Effect of streaks on Mack-mode waves*

The planar and oblique Mack-mode waves are modulated by the presence of the azimuthally periodic streaks. At any given, nonzero azimuthal wavenumber of the Mack-mode waves, there exists a pair of oblique modes with equal but opposite wave angles. For oblique Mack modes with wavenumbers equal to $m = m_{ST}$ (fundamental), $m = 1/2\, m_{ST}$ (subharmonic), and $m = 3/2\, m_{ST}$, the spanwise structure of the mode shape is phase locked to the streaks. As a result, there exist both varicose (symmetric) and sinuous (antisymmetric) modes with different amplification rates. For all other wavenumbers, there is no such phase locking, and hence, both oblique modes with the same value of m have the same amplification rate and their mode shapes satisfy the condition $\hat{\mathbf{q}}^-(\xi, \eta, \zeta) = \hat{\mathbf{q}}^+(\xi, \eta, -\zeta)$, where the superscripts $+$ and $-$ denote the signs of the spanwise components of phase velocities associated with the two modes constituting the pair.

Figure 8 shows the frequency dependence of spatial growth rates computed with quasiparallel PDE-based EVP at a fixed streamwise location of $\xi/L = 1.0$. Results are plotted for five different families of modes that can presumably be relevant in the presence of the streaks: MM_0, $\mathrm{MM}_{1/2,S}$, $\mathrm{MM}_{1/2,V}$, $\mathrm{MM}_{1,S}$, $\mathrm{MM}_{1,V}$, $\mathrm{MM}_{3/2,S}$, and $\mathrm{MM}_{3/2,V}$. The mode MM_0 reduces to a planar Mack-mode disturbance in the limit of $A \to 0$. Modes $\mathrm{MM}_{1/2,V}$ and $\mathrm{MM}_{1/2,S}$ correspond to oblique Mack-mode disturbances (with azimuthal wavenumber equal to one half of the streak spacing) of varicose and sinuous type, respectively. The fundamental varicose and sinuous modes, $\mathrm{MM}_{1,V}$ and $\mathrm{MM}_{1,S}$, respectively, correspond to oblique Mack-mode disturbances with azimuthal wavenumber equal to the streak spacing. Similarly, the modes $\mathrm{MM}_{3/2,V}$ and $\mathrm{MM}_{3/2,S}$ correspond to oblique Mack-mode disturbances with azimuthal wavenumber equal to 3/2 times the fundamental wavenumber, i.e., three Mack-mode wavelengths within two streak wavelengths, with the second suffix denoting the mode types as varicose and sinuous, respectively. Mode shapes for each family at frequencies corresponding to respective peak local growth rate are shown in figures 9(a) through 9(g) for a streak amplitude of $A = 0.10$. The varicose and sinuous characterizations of the modes correspond to the symmetry and antisymmetry mode shapes, respectively, with respect to the half symmetry plane of the streak ($\zeta = \lambda_{ST}/2$). Figure 8(a) shows a progressive reduction in the peak growth rate of MM_0 modes with increasing streak amplitude. Simultaneously, the growth rate curves are displaced toward lower frequencies because the MM_0 mode shape is concentrated on the crests of the modified flow (i.e., regions of increased boundary-layer thickness) as shown by figure 9(a). Similar to the MM_0 mode, both of the subharmonic modes ($\mathrm{MM}_{1/2,V}$ and $\mathrm{MM}_{1/2,S}$) have mode shape distributions that peak in the neighborhood of the crests (figures 9(b) and 9(c)). Accordingly, their peak growth frequencies decrease as the streak amplitude is increased. While the peak amplification rates of both subharmonic modes also decrease with an increasing streak amplitude, the stabilizing influence is substantially stronger for the sinuous mode $\mathrm{MM}_{1/2,S}$. Figure 8(c) indicates that the effect of the streaks is somewhat different in the case of the $\mathrm{MM}_{1,V}$ modes, which are strongest within the valley regions of the streaks. The growth rates of these $\mathrm{MM}_{1,V}$ modes initially increase with the streak amplitude parameter up to

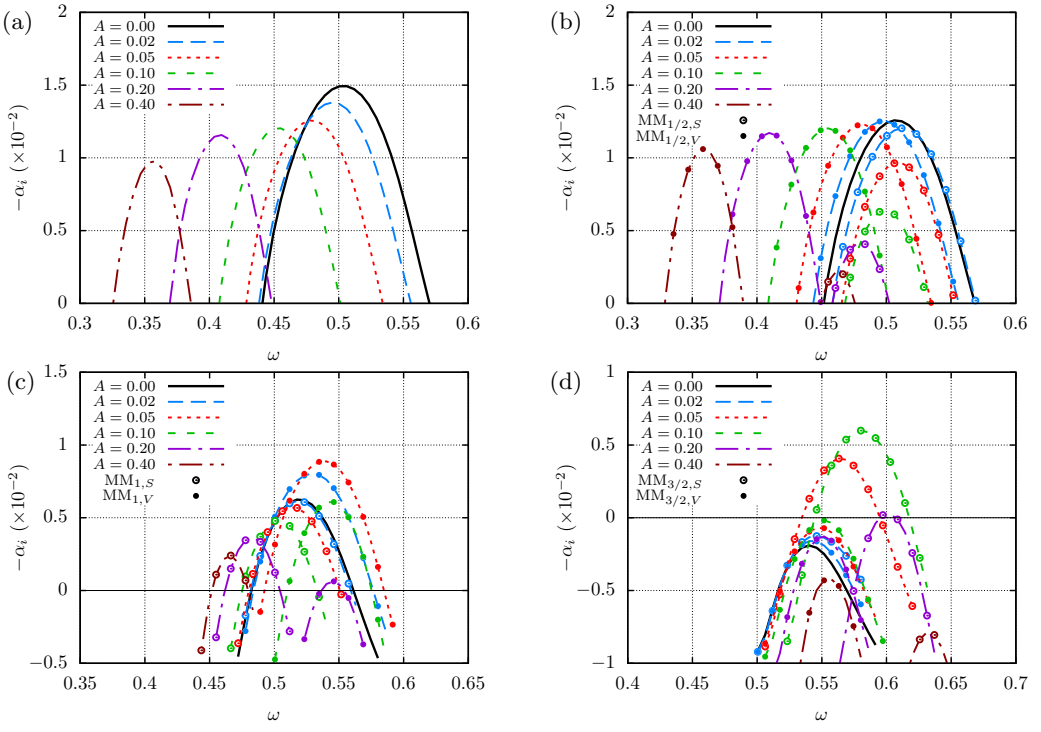

FIGURE 8. Spatial growth rates ($-\alpha_i$) of (a) planar Mack modes (MM_0), (b) oblique Mack modes with subharmonic ($m = 1/2\,m_{ST}$) sinuous ($\mathrm{MM}_{1/2,S}$) and varicose ($\mathrm{MM}_{1/2,V}$) mode shapes, (c) oblique Mack modes with fundamental ($m = m_{ST}$) sinuous ($\mathrm{MM}_{1,S}$) and varicose ($\mathrm{MM}_{1,V}$) mode shapes, and (d) oblique Mack modes with $m = 3/2\,m_{ST}$ sinuous ($\mathrm{MM}_{3/2,S}$) and varicose ($\mathrm{MM}_{3/2,S}$) mode shapes, for selected streak amplitudes at $\xi/L = 1.0$.

$A = 0.05$, and then decrease at higher A. Furthermore, the peak growth frequencies of the $\mathrm{MM}_{1,V}$ modes increase with A. In contrast, the streaks have a stabilizing influence on the $\mathrm{MM}_{1,S}$ modes (figure 9(d)) for all A. Finally, both the $\mathrm{MM}_{3/2,S}$ and $\mathrm{MM}_{3/2,V}$ modes are destabilized with streak amplitude parameter up to $A = 0.10$, although the varicose mode $\mathrm{MM}_{3/2,V}$ does not reach the neutral stability threshold, i.e., zero growth rate. The mode shapes of the modes $\mathrm{MM}_{3/2,S}$ and $\mathrm{MM}_{3/2,V}$ are shown in figures 9(f) and 9(g), respectively.

As explained before, the instability waves with wavenumbers different from those studied in figures 8 and 9 (namely, $m = 1/2\,m_{ST}$, m_{ST}, and $3/2\,m_{ST}$) are not phase locked by the presence of the streaks, and hence, both oblique modes with the same value of m have the same amplification rate and their mode shapes satisfy $\hat{\mathbf{q}}^-(\xi,\eta,\zeta) = \hat{\mathbf{q}}^+(\xi,\eta,-\zeta)$. Figure 10 shows the mode shape of the Mack mode wave with $m = 3/5\,m_{ST}$. The three perturbation wavelengths within the five streak wavelengths are visible in the real and imaginary parts of the perturbation. The streamwise velocity magnitude is rather similar to that corresponding to the $\mathrm{MM}_{1/2,S}$ plotted in figure 9(b), but differences in phase are observed in the real and imaginary parts of the mode shape components.

To characterize the overall effect of streaks on the amplification of the Mack-mode disturbances, we now examine the spatial evolution of fixed frequency planar and oblique Mack modes with the plane-marching PSE. The N-factor defined in Eq. (2.6) is used as a measure of the disturbance amplification. Figures 11(a) and 11(b) illustrate the N-factor

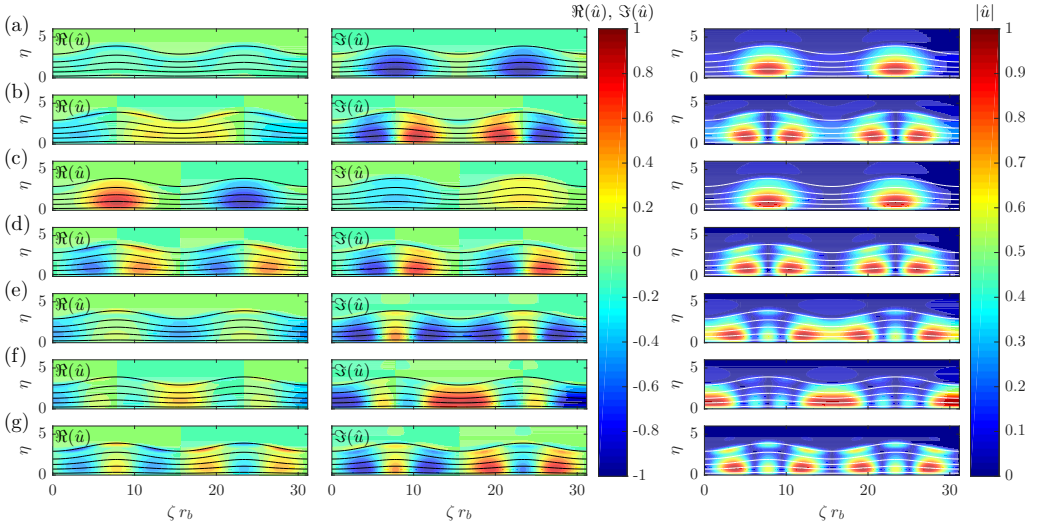

FIGURE 9. Isocontours of the real and imaginary parts and magnitude of streamwise velocity perturbations for $A = 0.10$ at $\xi/L = 1.0$ and frequencies (a) $\omega = 0.455$ for MM_0, (b) $\omega = 0.501$ for $\mathrm{MM}_{1/2,S}$, (c) $\omega = 0.455$ for $\mathrm{MM}_{1/2,V}$, (d) $\omega = 0.506$ for $\mathrm{MM}_{1,S}$, (e) $\omega = 0.546$ for $\mathrm{MM}_{1,V}$, (f) $\omega = 0.580$ for $\mathrm{MM}_{3/2,S}$, (g) $\omega = 0.552$ for $\mathrm{MM}_{3/2,V}$. The isolines of basic state streamwise velocity, $\bar{u} = 0 : 0.1 : 0.9$, are added for reference.

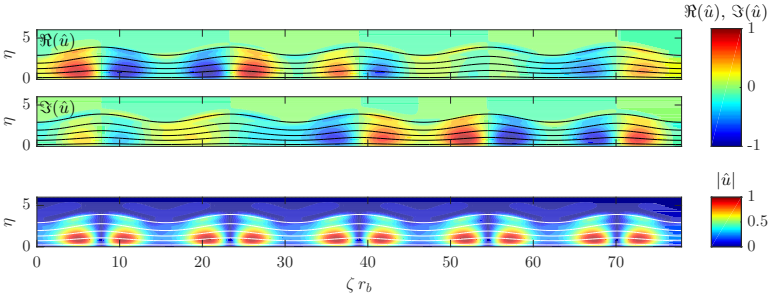

FIGURE 10. Isocontours of the real and imaginary parts and magnitude of streamwise velocity perturbation for $A = 0.10$ at $\xi/L = 1.0$ and frequency $\omega = 0.501$ for $\mathrm{MM}_{3/5}$. The isolines of basic state streamwise velocity, $\bar{u} = 0 : 0.1 : 0.9$, are added for reference.

evolution of the Mack modes with frequencies $\omega = 0.603$ and $\omega = 0.421$, respectively, for the unperturbed basic state ($A = 0.00$) and the perturbed flow with $A = 0.10$. Results for the unperturbed and pertubed flows include the planar Mack mode (MM_0) and oblique Mack modes with several values of m, i.e., $m = 1/4\, m_{ST}$ ($\mathrm{MM}_{1/4}$), $m = 1/3\, m_{ST}$ ($\mathrm{MM}_{1/3}$), $m = 1/2\, m_{ST}$ ($\mathrm{MM}_{1/2}$), $m = 3/5\, m_{ST}$ ($\mathrm{MM}_{3/5}$), $m = 2/3\, m_{ST}$ ($\mathrm{MM}_{2/3}$), and $m = m_{ST}$ (MM_1), as well as the sinuous (S) and varicose (V) mode types for the locked modes. As shown in figure 3, the disturbance frequency used in figure 11(a), $\omega = 0.603$, corresponds to the frequency of the planar Mack mode that reaches the largest N-factor, $N_{tr} = 14.7$, at the experimentally observed transition location, $\xi_{tr}/L = 0.85$ m. For the perturbed case with $A = 0.10$, the MM_0 disturbance frequency $\omega = 0.421$ that is used in figure 11(b), reaches the transition N-factor $N_{tr} = 14.7$ at the most upstream location, $\xi_{tr}/L = 1.39$. Figure 11(a) shows that for the unperturbed case, the maximum value of the N-factor is reached by the MM_0 mode and is $N = 14.97$. For the perturbed case, the peak N-factor is also reached by the MM_0 mode, but is drastically reduced to $N = 6.94$. For the perturbed flow case, the unlocked oblique modes $\mathrm{MM}_{1/4}$, $\mathrm{MM}_{1/3}$,

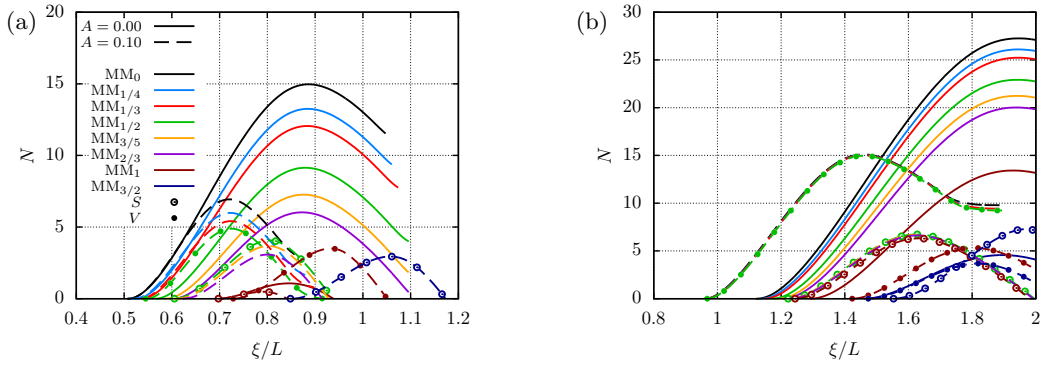

FIGURE 11. Evolution of N-factors with frequencies (a) $\omega = 0.603$ and (b) $\omega = 0.421$ of planar and selected oblique Mack-mode waves for the unperturbed boundary-layer flow ($A = 0.00$) and the perturbed boundary-layer flow with $A = 0.10$.

$MM_{3/5}$, and $MM_{2/3}$ experience a similarly stabilizing effect of the streaks as that found for the MM_0 mode and their N-factor curves remain below the N-factor curve of the MM_0 mode. The phase locked modes $MM_{1,V}$ and $MM_{3/2,S}$ are destabilized, although their peak N-factor values are approximately one half of the peak value corresponding to the N-factor of the MM_0 mode. Figure 11(b) shows that the peak N-factor values for the disturbance frequency $\omega = 0.421$ are reduced from $N = 25.26$ to $N = 15.11$ by the introduction of the streak. The N-factor curves of the $MM_{1/4}$, $MM_{1/3}$, $MM_{1/2,V}$ modes become nearly coincident but remain below the curve corresponding to the MM_0 mode. The rest of oblique Mack modes plotted in figure 11(b), i.e., $MM_{1/2,V}$, $MM_{3/5}$, $MM_{2/3}$, $MM_{1,S}$, $MM_{1,V}$, $MM_{3/2,S}$, and $MM_{3/2,V}$, are also less amplified than the MM_0. Therefore, we can conclude that the planar Mack mode, MM_0, dominates the instability characteristics of both the unperturbed and perturbed boundary-layer flows.

Herein, the primary mechanism for the effect of the streak on the reduced amplification of the planar Mack mode is investigated. Figures 12(a) and 12(b) illustrate the N-factor evolution of the MM_0 mode with frequencies $\omega = 0.603$ and $\omega = 0.421$, respectively, for the unperturbed basic state ($A = 0.00$) and the perturbed flow with $A = 0.10$. The extra three curves plotted in figures 12(a) and 12(b) indicate the N-factor evolution for the same frequencies using three "artificial" basic states: a two-dimensional basic state corresponding to the azimuthal average of the $A = 0.10$ flow, which corresponds to the unperturbed flow ($A = 0.00$) plus the mean flow distortion (MFD) due to the streak, $A = 0.00$+MFD, the perturbed flow with $A = 0.10$ minus the MFD of the perturbation, $A = 0.10-$MFD, and the two-dimensional profile at the half symmetry plane ($\zeta = \lambda_{ST}/2$) of the perturbed flow, $A = 0.10 : \zeta = \lambda/2$. These extra cases are introduced to understand the primary mechanism for the effect of the streak on the reduced amplification of the planar Mack mode. By comparing the N-factor of the first extra case ($A = 0.00$+MFD) with that for the unperturbed flow ($A = 0.00$), we can see that the MFD has a modestly stabilizing influence on the planar Mack mode, which is in qualitative agreement with the findings reported by Ren *et al.* (2016) for weak streaks ($As_u < 0.05$) and by Paredes *et al.* (2016*b*) for a broader range of streak amplitudes for a boundary-layer flow representative of wind tunnel conditions ($T_w/T_{w,ad} = 0.68$). However, the N-factor evolution for the second "artificial" case ($A = 0.10-$MFD) indicates a stronger stabilizing influence on the planar Mack mode by the three-dimensional modulation of the boundary layer, or, equally, the spanwise varying component of the stationary streak. The N-factor curve for the $A = 0.10-$MFD case closely approximates the result for the total perturbed

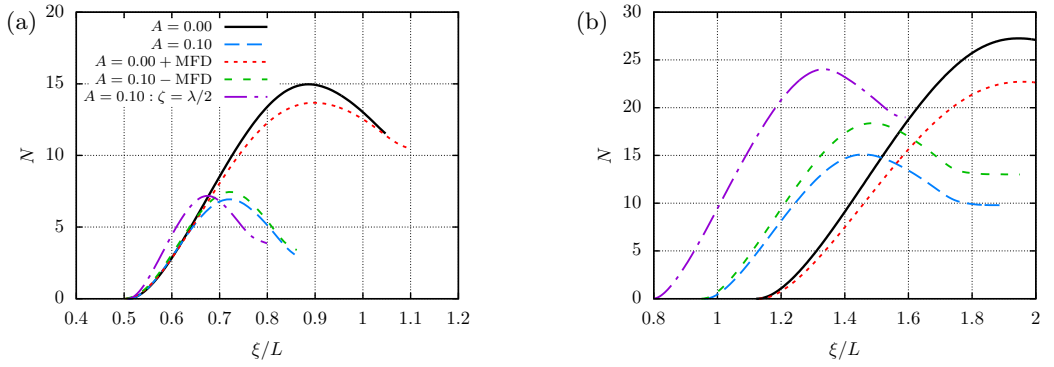

FIGURE 12. Evolution of N-factors of planar Mack-mode waves with frequencies (a) $\omega = 0.603$ and (b) $\omega = 0.421$ for the unperturbed basic state ($A = 0.00$), the perturbed basic state ($A = 0.10$), the unperturbed basic state plus the MFD of the $A = 0.10$ perturbation ($A = 0.10 + \mathrm{MFD}$), the perturbed basic state without the MFD ($A = 0.10 - \mathrm{MFD}$), and the $\zeta = \lambda_{ST}/2$ plane of the perturbed basic state ($A = 0.10 : \zeta = \lambda/2$).

flow ($A = 0.10$), i.e., has similar neutral locations and maximum peak amplifications. Therefore, the three-dimensional modulation of the boundary layer caused by the streaks dominates the overall modification of the instability characteristics of the planar Mack-mode waves. Because the MM_0 mode shape is concentrated on the crests of the undulating velocity contours of the modified flow (figure 9(a)), the analysis of the third "artificial" case ($A = 0.10 : \zeta = \lambda/2$) intends to resolve whether the instability characteristics of the boundary layer along the half symmetry plane reflects the instability features of the total flow field. Figures 12(a) and 12(b) show that as the streak amplitude becomes significant for $\xi/L > 0.5$ (figure 5), the N-factor curve of the $A = 0.10 : \zeta = \lambda/2$ case strongly differs from that corresponding to the $A = 0.10$ case, which implies that the three-dimensional effects need to be considered.

Finally, to further understand the dominant mechanism of the instability modes, the production terms associated with the local kinetic energy transfer as a function of the streamwise location are calculated; see Malik *et al.* (1999) and Paredes *et al.* (2017*a*) for further details. Figures 13(a) and 13(b) show the evolution of the normalized production terms associated with the streamwise velocity gradients in the three directions (ξ, η, ζ) for disturbance frequencies $\omega = 0.603$ and $\omega = 0.421$, respectively. These terms are written as

$$Pu_\xi(\xi) = -\int_\zeta \int_\eta \Re(\hat{u}\hat{u}^c)\bar{\rho}\bar{u}_\xi h_\xi h_\zeta \,\mathrm{d}\eta\,\mathrm{d}\zeta, \tag{3.6}$$

$$Pu_\eta(\xi) = -\int_\zeta \int_\eta \Re(\hat{u}\hat{v}^c)\bar{\rho}\bar{u}_\eta h_\xi h_\zeta \,\mathrm{d}\eta\,\mathrm{d}\zeta, \tag{3.7}$$

$$Pu_\zeta(\xi) = -\int_\zeta \int_\eta \Re(\hat{u}\hat{w}^c)\bar{\rho}\bar{u}_\zeta h_\xi h_\zeta \,\mathrm{d}\eta\,\mathrm{d}\zeta, \tag{3.8}$$

where the superscript c denotes complex conjugate. Figures 13(a) and 13(b) show that the production term associated with the wall-normal gradient clearly dominates for both the unperturbed and perturbed cases, because the streamwise and azimuthal terms are negligible. Furthermore, the Pu_η term for the perturbed boundary layer flow remains positive over a relatively shorter streamwise domain, which explains the shorter range of amplification and the lower N-factor peak of the MM_0 mode observed in figures 12(a) and 12(b).

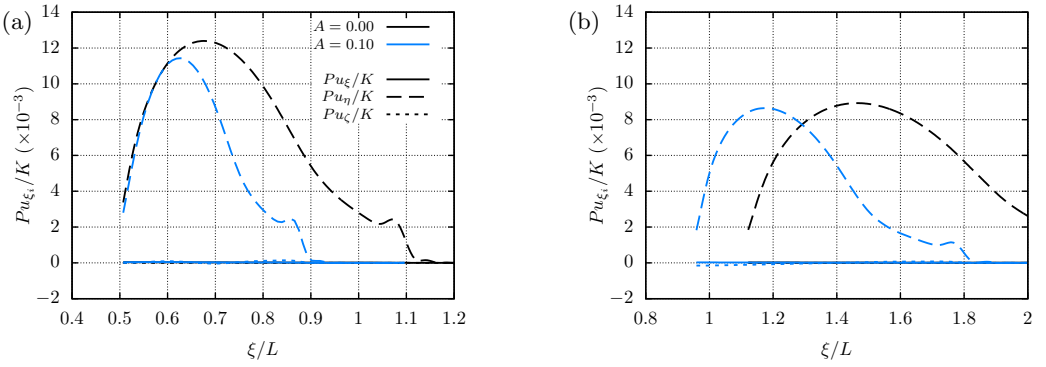

FIGURE 13. Evolution of the ratio between the production terms associated with the streamwise velocity gradients and the kinetic energy of the planar Mack-mode waves with frequencies (a) $\omega = 0.603$ and (b) $\omega = 0.421$.

3.4.2. *Streak instabilities*

In the previous subsections, we discussed the effect of streaks on the unstable eigenmodes of the unperturbed boundary layer. However, as the streak amplitude is increased, some of the stable (i.e., damped) modes of the original, axisymmetric boundary layer become increasingly less stable, and eventually, cross over into the unstable portion of the spectrum. Indeed, at large enough streak amplitudes, these streak instabilities (denoted as SI modes following the nomenclature of Li *et al.* (2016)) can become the most amplified modes, and hence, can dominate the process of laminar-turbulent transition. The PDE-based EVP analysis is used to obtain the growth rates (figure 14) and eigenfunctions (figure 15) of subharmonic and fundamental sinuous and varicose streak instability modes ($\mathrm{SI}_{1/2,S}$, $\mathrm{SI}_{1/2,V}$, $\mathrm{SI}_{1,S}$, and $\mathrm{SI}_{1,V}$) at $\xi/L = 1.0$ for the selected streak amplitudes. Figure 14 shows that the $\mathrm{SI}_{1/2,S}$ mode is the first streak instability mode to become unstable for $A = 0.20$. The $\mathrm{SI}_{1/2,S}$ is also the most unstable streak instability mode for streak amplitude parameters $A \leqslant 0.40$. The $\mathrm{SI}_{1,S}$ becomes unstable for $A = 0.30$ and is the most amplified mode for $A = 0.50$. Varicose modes, $\mathrm{SI}_{1/2,V}$ and $\mathrm{SI}_{1,V}$ become unstable for $A = 0.50$. Summarizing, the $\mathrm{SI}_{1/2,S}$ mode is the most unstable mode for moderate streak amplitudes and, therefore, may play an important role in the transition process. Mode shapes for each family at frequencies corresponding to peak local growth rate are shown in figures 15(a) through 15(d) for a streak amplitude parameter of $A = 0.50$. The streamwise velocity magnitude isocontours are rather similar between the fundamental and subharmonic sinuous modes, $\mathrm{SI}_{1/2,S}$ and $\mathrm{SI}_{1,S}$, as well as between the varicose modes, $\mathrm{SI}_{1/2,V}$ and $\mathrm{SI}_{1,V}$. These modes differ in the phase, which is observed in the real and imaginary parts of the mode shape perturbation.

3.4.3. *Overall effect on predicted transition onset*

The overall effect of the streaks on the instability characteristics of the hypersonic boundary-layer flow is summarized in figures 16(a) and 16(b), where the neutral stability curves and the N-factor envelopes, respectively, of the MM_0 and $\mathrm{SI}_{1/2,S}$ modes are plotted for selected streak amplitudes. Figure 16(a) shows how the streaks affect the range of unstable frequencies. As explained in 3.4.1, the neutral stability curves are displaced toward lower frequencies because the MM_0 mode shape concentrates on the crests of the modified flow (i.e., regions of increased boundary-layer thickness) as shown by figure 9(a). The sinuous subharmonic streak instabilities, which arise from the stable oblique first-mode disturbance with the same azimuthal wavelength, as documented by Paredes *et al.*

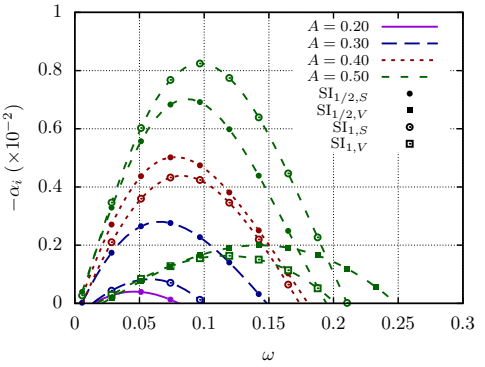

FIGURE 14. Spatial growth rates ($-\alpha_i$) of streak instability modes ($\mathrm{SI}_{1/2,S}$, $\mathrm{SI}_{1/2,V}$, $\mathrm{SI}_{1,S}$, and $\mathrm{SI}_{1,V}$) for selected streak amplitudes at $\xi/L = 1.0$.

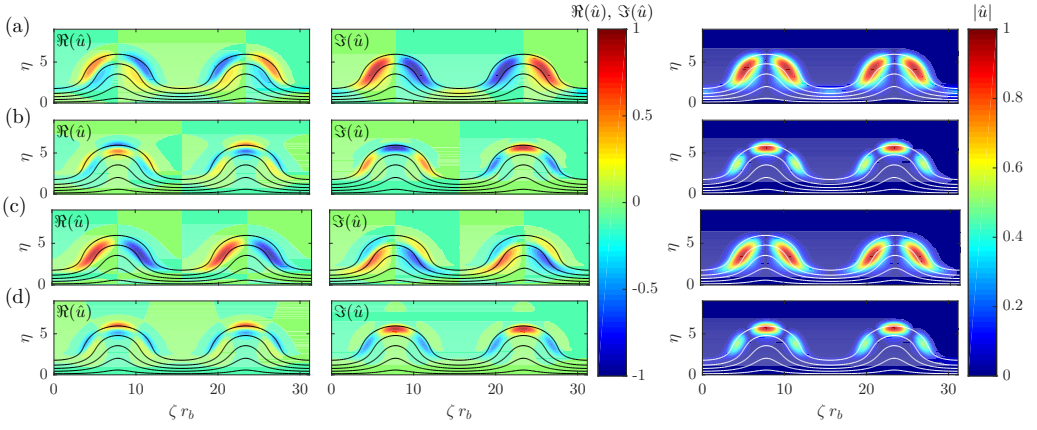

FIGURE 15. Isocontours of real and imaginary parts and magnitude of streamwise velocity perturbations for $A = 0.50$ at $\xi/L = 1.0$ and frequencies (a) $\omega = 0.0853$ for $\mathrm{SI}_{1/2,S}$, (b) $\omega = 0.142$ for $\mathrm{SI}_{1/2,V}$, (c) $\omega = 0.0967$ for $\mathrm{SI}_{1,S}$, and (d) $\omega = 0.119$ for $\mathrm{SI}_{1,V}$.

(2016*c*,*b*, 2017*a*) for supersonic and hypersonic boundary layer flows, become unstable for streak amplitude parameter $A = 0.20$, with associated frequencies lower than those associated to the MM_0 mode. For each of the selected streak amplitudes, the stability regions of the MM_0 and $\mathrm{SI}_{1/2,S}$ modes are separate from each other.

The primary focus of this work corresponds to the stabilizing effect of streaks on Mack-mode disturbances, which have been shown to cause transition in the present flow configuration (Li *et al.* 2015*a*). For the conditions of the experiment (Kimmel *et al.* 2015), transition onset in the unperturbed cone boundary layer was measured to occur near $\xi_{tr}/L = 0.85$, where the peak N-factor of the MM_0 modes is $N_{tr} = 14.7$. Selecting this value as the transition threshold, figure 16(b) shows how the transition onset due to MM_0 modes would be displaced downstream by the introduction of the finite-amplitude optimal disturbances. For the highest streak amplitude considered herein ($A = 0.40$ with $\max(As_u) = 0.34$), the MM_0 modes reach the threshold N-factor at $\xi_{tr,MM_0}/L = 1.84$, although the sinuous, subharmonic streak instability $\mathrm{SI}_{1/2,S}$ reaches the threshold N-factor at $\xi_{tr,SI_{1/2,S}}/L = 1.76$. Assuming that the threshold N-factor is equivalent for Mack mode and streak instabilities, the laminar flow region would be 2.07 times larger than for the unperturbed case. These results for high altitude conditions present an interesting comparison with the findings by Paredes *et al.* (2016*b*) for a 7° half-

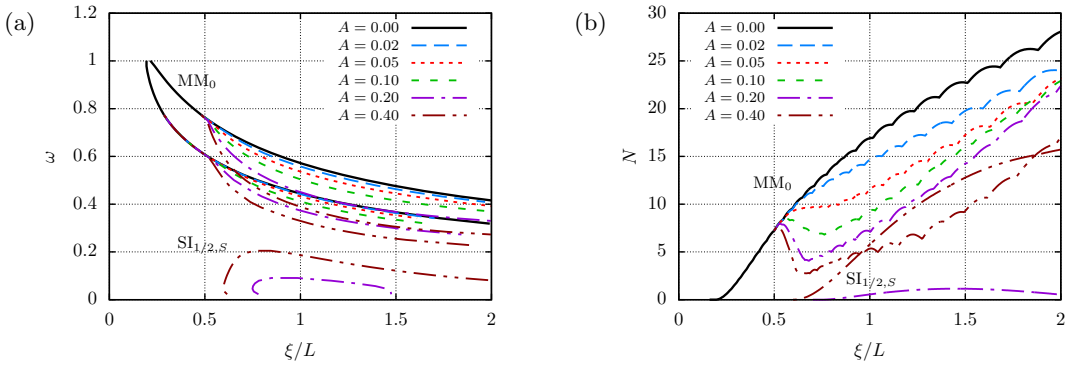

FIGURE 16. (a) Neutral stability curves and (b) N-factor envelopes for planar Mack-mode disturbances (MM$_0$) and sinuous, subharmonic streak instability modes (SI$_{1/2,S}$).

angle circular cone at the flow conditions of a ground test experiment in the VKI H3 hypersonic tunnel (Grossir *et al.* 2015), namely $M_\infty = 6$, $Re' = 18\times10^6$ m^{-1}, $T_\infty = 60.98$ K, and wall-to-adiabatic temperature ratio equal to $T_w/T_{w,ad} = 0.68$. In the case of Paredes *et al.* (2016*b*), the higher value of the $T_w/T_{w,ad}$ allows for the growth of oblique first-mode instability waves, which are destabilized by the presence of the streaks and eventually become the streak instability modes. The amplification due to the modulated unstable first-mode waves leads to a lower threshold streak amplitude beyond which streak instability becomes the dominant cause for the onset of transition.. Paredes *et al.* (2016*b*) predicted that the subharmonic sinuous mode dominates the transition onset above $A \approx 0.20$ for the ground test case with $T_w/T_{w,ad} = 0.68$, while the streak amplitude analogous value of threshold for the flight test case with $T_w/T_{w,ad} = 0.35$ is $A \approx 0.40$ as observed in figure 16(b).

The N-factor threshold to cause transition can be lower in the presence of the streaks than that in the uncontrolled case. The present analysis is solely based on the effect of the streaks on the linear amplification stage and because of the role of the streaks (or the device used to excite those streaks) on the receptivity and/or nonlinear phases of transition, lower N-factors at the onset of transition can be possible. However, the results in figure 16(b) suggest that even if the transition N-factor for the boundary layer with streaks were to be as low as $N = 10$ (as against the value of $N = 14.7$ in the uncontrolled case), transition onset may still be delayed until $\xi/L = 1.34$ for a streak amplitude of $A = 0.30$.

The present results show a potential increase in the length of the laminar flow that is comparable to the length of the laminar region in the unperturbed case, i.e., the laminar flow acreage is potentially doubled. Considering that the ratio of local skin friction coefficients for turbulent and laminar flows is in the range of $c_{f,tur}/c_{f,lam} \in [5, 7]$ (Schlichting 1979), the maximum total skin friction reduction for the present geometry with a total length corresponding to $Re_{L_c} = 26.84 \times 10^6$, at the present flow conditions ($M_\infty = 5.3$, $Re' = 13.42 \times 10^6$ m^{-1}, $T_w/T_{w,ad} = 0.35$) and with a transition threshold of $N = 14.7$, would be of the order of 60% relative to the unperturbed case.

3.4.4. *Effect of streak wavenumber on transition onset*

A parameter study for additional streak wavenumbers m_{ST} is conducted to help with identifying the optimal flow control setting to maximize the transition delay for a given flow configuration. Figure 17(a) shows the evolution of N-factor envelopes for the unperturbed boundary layer ($A = 0.00$) and the perturbed boundary layers for a streak

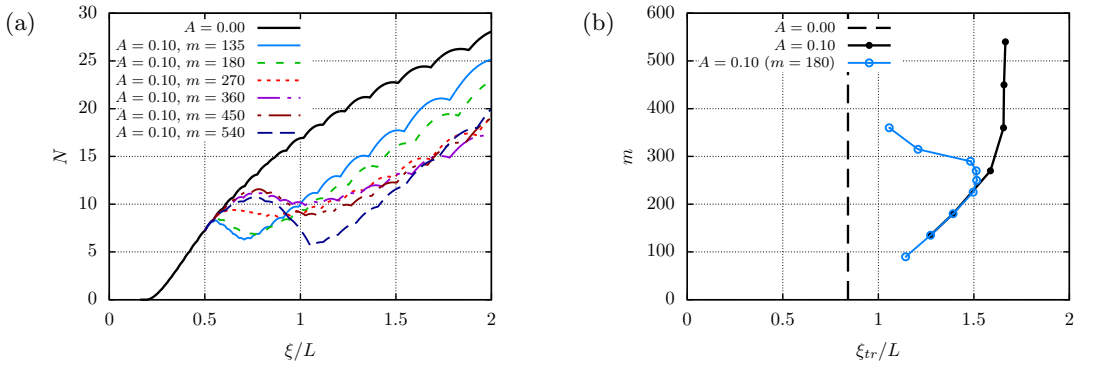

FIGURE 17. (a) N-factor envelopes for the unperturbed boundary-layer flow ($A = 0.00$) and for perturbed boundary-layer flows with $A = 0.10$ and selected streak azimuthal wavenumbers $m_{ST} = 135$, 180, 270, 360, 450, and 540. (b) Effect of predicted transition location with streak azimuthal wavenumber for same streak amplitude parameter $A = 0.10$, and for same initial disturbance amplitude A_0 corresponding to $A = 0.10$ for $m_{ST} = m_{op} = 180$. The experimentally measured transition location for the unperturbed case ($A = 0.00$) is included. The suffix ST is excluded in the figures for simplification.

amplitude parameter of $A = 0.10$ and selected azimuthal wavenumbers. Note that the initial streak disturbance amplitude A_0 is different for each perturbed case with selected azimuthal wavenumbers following Eq. (3.4). The N-factor envelope curves show a strong effect of the streak azimuthal wavenumber. For the azimuthal wavenumber ($m_{ST} = 135$) smaller than the optimal streak wavenumber ($m_{ST} = m_{op} = 180$), the N-factor values are larger than those corresponding to $m_{ST} = m_{op}$ along most of the streamwise domain, but slightly smaller near the initial disturbance location ($\xi_0/L = 0.5$). For the present configuration, streaks with $m_{ST} < m_{op}$ would be less effective for transition delay than $m_{ST} = m_{op}$. For azimuthal streak wavenumbers larger than m_{op}, the effect of the streaks is weaker near the initial disturbance location, resulting in larger N-factor values than those corresponding to the $m_{ST} = m_{op}$ case, but the N-factor values decrease further downstream and the N-factor envelopes for $m_{ST} > m_{op}$ remains below that corresponding to $m_{ST} = m_{op}$ along most of the domain. Streak instabilities were not found for any of the selected cases, even though the initial disturbance amplitude at these suboptimal wavenumbers must be larger than that for $m_{ST} = m_{op}$ in order to reach the same maximum streak amplitude. Therefore, for the same value of maximum streak amplitude, streaks with azimuthal wavenumbers larger than that are larger than the wavenumber corresponding to optimal transient growth are likely to result in a longer delay in the onset of transition. To help determine the most convenient streak azimuthal wavenumber for transition delay, figure 17(b) shows the predicted transition location as a function of the azimuthal wavenumbers for optimal disturbances initiated at $\xi/L = 0.5$ with same streak amplitude parameter $A = 0.10$ and with same initial amplitude A_0, which is set to the relatively modest value for $A = 0.10$ with $m_{ST} = m_{op} = 180$. Results show that the streaks with $m_{ST} = 256$ ($m_{ST} = 1.42\, m_{op}$) lead to a further downstream displacement of the transition location with same initial amplitude; specifically, the predicted transition location is $\xi_{tr}/L = 1.39$ for $m_{ST} = m_{op} = 180$ and $\xi_{tr}/L = 1.52$ for $m_{ST} = 256$ with same initial amplitude A_0.

4. Summary and concluding remarks

Optimal growth theory based on the stationary form of parabolized stability equations (PSE) is used to identify the range of modulating wavenumbers that would benefit the most from the intrinsic "lift-up" mechanisms within a high-speed boundary-layer flow over a 7° half-angle circular cone at zero angle of attack. The plane-marching PSE have been used to monitor the nonlinear disturbance evolution of finite-amplitude, linearly optimal perturbations. Subsequently, the linear stability characteristics of the perturbed streaky boundary-layer flow are studied using the linear form of the plane-marching PSE. The present results have demonstrated that the introduction of finite-amplitude optimal growth streaks in a Mach 5.3 axisymmetric flow over a cone at realistic flight conditions from the HIFiRE-1 experiment will reduce the peak linear amplification of boundary-layer instabilities, indicating the possibility of a delayed onset of laminar-turbulent transition. The current predictions show that the planar Mack-mode waves are the most amplified instabilities for both the unperturbed and perturbed cases up to a threshold amplitude of the stationary streaks. A detailed analysis of the primary mechanism for the effect of the streaks on the reduced amplification of the planar Mack modes provides further evidence that the MFD of the nonlinear stationary streak perturbation has a stabilizing effect on the Mack modes as previously reported by Ren *et al.* (2016) for small streak amplitudes and by Paredes *et al.* (2016*b*) for a broad range of streak amplitudes. More interestingly, however, the present calculations demonstrate that the spanwise varying component of the stationary streak has an even larger effect of the amplification characteristics of the Mack modes. Yet, in general, the production of disturbance kinetic energy associated with the boundary layer instabilities is dominated by the wall-normal gradients of the boundary layer flow with or without the streaks. For sufficiently large streak amplitudes, intrinsic instabilities of the streaks can reach the threshold N-factor for transition onset before the Mack-mode instabilities.

The results indicate that, if suitable stationary disturbances can be excited in the originally axisymmetric boundary-layer flow, then the net stabilization of planar Mack-mode instabilities due to the stationary streaks may lead to a notable delay in transition onset, provided that the N-factor values correlating with transition onset remain similar in both unperturbed and perturbed cases. The streaks with azimuthal wavenumber corresponding to the optimal transient growth yield a downstream movement of the laminar-turbulent transition onset that is comparable to the uncontrolled transition length, which translates into a reduction of the total skin friction of the order of the 60% relative to the uncontrolled case. Furthermore, the parametric study for additional streak wavenumbers has shown that a larger streak wavenumber of approximately 1.4 times the optimal growth value, may actually result in an increased delay in transition.

Detailed laboratory experiments are required to establish the effect of streaks, if any, on the N-factor correlation. The physical source responsible for the excitation of transient growth disturbances has not been addressed in this study and, in turn, the effect of this source on the generation (i.e., receptivity) of the unsteady modal instabilities is also not addressed in the present investigation. A study of both these aspects would represent an important extension of the present work.

This research was sponsored by the NASA Transformational Tools and Technologies (TTT) Project of the Transformative Aeronautics Concepts Program under the Aeronautics Research Mission Directorate. Resources supporting this work were provided by the NASA High-End Computing (HEC) Program through the NASA Advanced Supercomputing (NAS) Division at Ames Research Center.

REFERENCES

Andersson, P., Brandt, L., Bottaro, A. & Henningson, D.S. 2001 On the breakdown of boundary layer streaks. *J. Fluid Mech.* **428**, 29–60.

Bagheri, S. & Hanifi, A. 2007 The stabilizing effect of streaks on Tollmien-Schlichting and oblique waves: A parametric study. *Phys. Fluids* **19**, 078103–1–078103–4.

Boiko, A.V., Westin, K.J.A., Klingmann, B.G.B., Kozlov, V.V. & Alfredsson, P.H. 1994 Experiments in a boundary layer subjected to free stream turbulence. Part 2. The role of TS-waves in the transition process. *J. Fluid Mech.* **281**, 219–245.

Choudhari, M., Li, F. & Edwards, J. 2009 Stability analysis of roughness array wake in a high-speed boundary layer. AIAA Paper 2009-0170.

Choudhari, M., Li, F., Paredes, P. & Duan, L. 2017 Computations of crossflow instability in hypersonic boundary layers. AIAA Paper 2017-4300.

Choudhari, M., Li, F., Paredes, P. & Duan, L. 2018 Nonlinear evolution and breakdown of azimuthally compact crossflow vortex pattern over a yawed cone. AIAA Paper 2018-1823.

Cossu, C. & Brandt, L. 2002 Stabilization of Tollmien-Schlichting waves by finite amplitude optimal streaks in the Blasius boundary layer. *Phys. Fluids* **14** (8), L57–L60.

De Tullio, N., Paredes, P., Sandham, N.D. & Theofilis, V. 2013 Roughness-induced instability and breakdown to turbulence in a supersonic boundary-layer. *J. Fluid Mech.* **735**, 613–646.

Fong, K.D., Wang, X., Huang, Y., Zhong, X., McKiernan, G.R., Fisher, R.A. & Schneider, S.P. 2015 Second mode suppression in hypersonic boundary layer by roughness: design and experiments. *AIAA J.* **53** (10), 3138–3143.

Fong, K.D., Wang, X. & Zhong, X. 2014 Numerical simulation of roughness effect on the stability of a hypersonic boundary layer. *Compt. Fluids* **96**, 350–367.

Fransson, J.H., Talamelli, A., Brandt, L. & Cossu, C. 2006 Delaying transition to turbulence by a passive mechanism. *Phys. Rev. Lett.* **96**, 064501.

Fujii, K. 2006 Experiment of the two-dimensional roughness effect of hypersonic boundary-layer transition. *J. Spacecraft Rockets* **43** (4), 731–738.

Grossir, G., Musutti, D. & Chazot, O. 2015 Flow characterization and boundary layer transition studies in VKI hypersonic facilities. AIAA Paper 2015-0578.

Hanifi, A., Schmid, P.J. & Henningson, D.S. 1996 Transient growth in compressible boundary layer flow. *Phys. Fluids* **8**, 51–65.

Hermanns, M. & Hernández, J. A. 2008 Stable high-order finite-difference methods based on non-uniform grid point distributions. *Int. J. Numer. Meth. Fluids* **56**, 233–255.

Holloway, P.F. & Sterrett, J.R. 1964 Effect of controlled surface roughness on boundary-layer transition and heat transfer at Mach number of 4.8 and 6.0. NASA TR-D-2054.

James, C.S. 1959 Boundary-layer transition on hollow cylinders in supersonic free flight as affected by Mach number and a screwthread type of surface roughness. NASA TR-Memo-1-20-59A.

Kimmel, R., Adamczak, D., Gaitonde, D., Rougeux, A. & Haynes, J.R. 2007 HIFiRE-1 boundary layer transition experiment design. AIAA Paper 2007-0534.

Kimmel, R., Adamczak, D., Paull, A., Paull, R., Shannon, J., Pietsch, R., Frost, M. & Alesi, H. 2015 HIFiRE-1 ascent-phase boundary-layer transition. *J. Spacecraft Rockets* **52** (1), 217–230.

Klebanoff, P.S. 1971 Effect of free-stream turbulence on the laminar boundary layer. *Bull. Am. Phys. Soc.*, **16**, 1323.

Li, F., Choudhari, M., Chang, C.L., Kimmel, R., Adamczak, D. & Smith, M. 2015*a* Transition analysis for the ascent phase of HIFiRE-1 flight experiment. *J. Spacecraft Rockets* **52** (5), 1283–1293.

Li, F., Choudhari, M., Chang, C.-L., Greene, P. & Wu, M. 2010 Development and breakdown of Gortler vortices in high speed boundary layers. AIAA Paper 2010-0705.

Li, F., Choudhari, M., Paredes, P. & Duan, L. 2015*b* Secondary instability of stationary crossflow vortices in Mach 6 boundary layer over a circular cone. NASA TM-2015-218997.

Li, F., Choudhari, M., Paredes, P. & Duan, L. 2016 High-frequency instabilities of stationary crossflow vortices in a hypersonic boundary layer. *Phys. Rev. Fluids* **1**, 053603–1–32.

Litton, D.K., Edwards, J.R. & White, J.A. 2003 Algorithmic enhancements to the VULCAN Navier-Stokes solver. AIAA Paper 2003-3979.

Mack, L.M. 1984 Boundary layer linear stability theory. In *AGARD–R–709 Special course on stability and transition of laminar flow*, pp. 3.1–3.81.

Mack, L. M. 1969 Boundary layer stability theory. *Tech. Rep.* 900-277. Jet Propulsion Lab., Pasadena, CA.

Malik, M.R., Li, F., Choudhari, M.M. & Chang, C.-L. 1999 Secondary instability of crossflow vortices and swept-wing boundary-layer transition. *J. Fluid Mech.* **399**, 85–115.

Paredes, P. 2014 Advances in global instability computations: from incompressible to hypersonic flow. PhD thesis, Universidad Politécnica de Madrid.

Paredes, P., Choudhari, M.M. & Li, F. 2016*a* Nonlinear transient growth and boundary layer transition. AIAA Paper 2016-3956.

Paredes, P., Choudhari, M. & Li, F. 2016*b* Transition delay in hypersonic boundary layers via optimal perturbations. NASA TM-2016-219210.

Paredes, P., Choudhari, M.M. & Li, F. 2016*c* Transition due to streamwise streaks in a supersonic flat plate boundary layer. *Phys. Rev. Fluids* **1**, 083601–1–23.

Paredes, P., Choudhari, M.M. & Li, F. 2017*a* Instaiblity wave-streak interactions in a supersonic boundary layer. *J. Fluid Mech.* **831**, 524–553.

Paredes, P., Choudhari, M. & Li, F. 2017*b* Stabilization of hypersonic boundary layers by linear and nonlinear optimal perturbations. AIAA Paper 2017-3634.

Paredes, P., Choudhari, M. & Li, F. 2017*c* Transient growth and streak instabilities on a hypersonic blunt body. AIAA Paper 2017-0066.

Paredes, P., Choudhari, M.M., Li, F. & Chang, C.-L. 2016*d* Optimal growth in hypersonic boundary layers. *AIAA J.* **54** (10), 3050–3061.

Paredes, P., De Tullio, N., Sandham, N. D. & Theofilis, V. 2015*a* Instability study of the wake behind a discrete roughness element in a hypersonic boundary layer. In *Instability and Control of Massively Separated Flows* (ed. Vassilis Theofilis & Julio Soria), pp. 91–96. Springer International Publishing.

Paredes, P., Hanifi, A., Theofilis, V. & Henningson, D. 2015*b* The nonlinear PSE-3D concept for transition prediction in flows with a single slowly-varying spatial direction. *Procedia IUTAM* **14C**, 35–44.

Paredes, P., Hermanns, M., Le Clainche, S. & Theofilis, V. 2013 Order 10^4 speedup in global linear instability analysis using matrix formation. *Comput. Meth. Appl. Mech. Eng.* **253**, 287–304.

Pralits, J.O., Airiau, C., Hanifi, A. & Henningson, D.S. 2000 Sensitivity analysis using adjoint parabolized stability equations for compressible flows. *Flow Turbul. Combust.* **65**, 183–210.

Ren, J., Fu, S. & Hanifi, A. 2016 Stabilization of the hypersonic boundary layer by finite-amplitude streaks. *Phys. Fluids* **28**, 024110–1–16.

Rumsey, C.L., Biedron, R.T. & Thomas, J.L. 1997 CFL3D: Its history and some recent applications. NASA TM-112861.

Schlichting, H. 1979 *Boundary Layer Theory*. McGraw-Hill.

Schmid, P. J. 2007 Nonmodal stability theory. *Annu. Rev. Fluid Mech.* **39**, 129–162.

Shahinfar, S., Sattarzadeh, S.S., Fransson, J.H. & Talamelli, A. 2012 Revival of classical vortex generators now for transition delay. *Phys. Rev. Lett.* **109**, 074501.

Tumin, A. & Reshotko, E. 2003 Optimal disturbances in compressible boundary layers. *AIAA J.* **41**, 2357–2363.

Vermeersch, O. & Arnal, D. 2010 Klebanoff-mode modeling and bypass-transition prediction. *AIAA J.* **48** (11), 2491–2500.

Zuccher, S., Tumin, A. & Reshotko, E. 2006 Parabolic approach to optimal perturbations in compressible boundary layers. *J. Fluid Mech.* **556**, 189–216.